



**HAL**  
open science

## **Sr- and Fe-substituted LaMnO<sub>3</sub> Perovskite: Fundamental insight and possible use in asymmetric hybrid supercapacitor**

P. Muhammed Shafi, Debananda Mohapatra, V. Pradeep Reddy, Ganesh Dhakal, Deivasigamani Ranjith Kumar, Dirk Tuma, Thierry Brousse, Jae-Jin Shim

### ► To cite this version:

P. Muhammed Shafi, Debananda Mohapatra, V. Pradeep Reddy, Ganesh Dhakal, Deivasigamani Ranjith Kumar, et al.. Sr- and Fe-substituted LaMnO<sub>3</sub> Perovskite: Fundamental insight and possible use in asymmetric hybrid supercapacitor. *Energy Storage Materials*, 2022, 45, pp.119-129. 10.1016/j.ensm.2021.11.028 . hal-03658089

**HAL Id: hal-03658089**

**<https://hal.science/hal-03658089>**

Submitted on 13 Jul 2022

**HAL** is a multi-disciplinary open access archive for the deposit and dissemination of scientific research documents, whether they are published or not. The documents may come from teaching and research institutions in France or abroad, or from public or private research centers.

L'archive ouverte pluridisciplinaire **HAL**, est destinée au dépôt et à la diffusion de documents scientifiques de niveau recherche, publiés ou non, émanant des établissements d'enseignement et de recherche français ou étrangers, des laboratoires publics ou privés.

# Sr- and Fe-substituted LaMnO<sub>3</sub> Perovskite: Fundamental Insight and Possible Use in Asymmetric Hybrid Supercapacitor

*P. Muhammed Shafi,<sup>a</sup> Debananda Mohapatra,<sup>a</sup> V. Pradeep Reddy,<sup>b</sup> Ganesh Dhakal,<sup>a</sup> Deivasigamani Ranjith Kumar,<sup>a</sup> Dirk Tuma,<sup>c</sup> Thierry Brousse,<sup>d,e,\*</sup> Jae-Jin Shim<sup>a,\*</sup>*

<sup>a</sup> School of Chemical Engineering, Yeungnam University, Gyeongsan, Gyeongbuk 38541, Republic of Korea

<sup>b</sup> Department of Physics, Vel Tech Rangarajan Dr. Sagunthala R&D Institute of Science and Technology, Chennai 600062, India

<sup>c</sup> BAM Federal Institute for Materials Research and Testing, 12200 Berlin, Germany

<sup>d</sup> Université de Nantes, CNRS, Institut des Matériaux Jean Rouxel, IMN, F-44000 Nantes, France

<sup>e</sup> Réseau sur le Stockage Electrochimique de l'Energie (RS2E), CNRS FR 3459, 33 rue Saint Leu, 80039 Amiens Cedex, France

Keywords: Perovskite oxide, Cationic substitutions, Mixed ionic-electronic conductivity, Graphitic carbon nano-onion, Hybrid device, Asymmetric supercapacitor.

Abstract:

The symmetry or structural stability of ABO<sub>3</sub>-type perovskite oxides depends largely on the size of 'A' and 'B' cations, which determines the material properties. The partial substitution of these cations may be used to tune these properties. The ionic sizes and valence states of the cations play an important role in improving the properties of perovskite. In this study, the substitution of La<sup>3+</sup> with Sr<sup>2+</sup> with a larger ionic radius and Mn<sup>3+</sup> with Fe<sup>3+</sup> with a similar ionic radius favored both the crystal symmetry and the mixed ionic-electronic conductivity of the perovskite. Electrodes based on La<sub>0.7</sub>Sr<sub>0.3</sub>Mn<sub>0.5</sub>Fe<sub>0.5</sub>O<sub>3</sub> (LSMFO55) exhibited a faradaic behavior with a specific capacity of 330 C g<sup>-1</sup> (92 mAh.g<sup>-1</sup>) at 12C rate, while this electrode

maintained a capacity of  $259 \text{ C g}^{-1}$  at  $240\text{C}$  (charge or discharge in 15s). Additionally, exohedral carbon nano-onions (CNO) were introduced as a negative electrode to design an asymmetric hybrid supercapacitor (AHS) with a widened cell voltage. The use of CNO as a negative electrode in the AHS improved the rate capability drastically compared to the use of rGO. This device maintained a good energy density even at an extra-high charging rate ( $600\text{C}$ ) owing to its outstanding rate capability. The high-rate performance of the LSMFO55//CNO AHS can be elucidated by successful fabrication with a mixed ionic-electronic conductive positive electrode and a CNO negative electrode. Tuning the electronic and ionic conductivities by cationic substitution and the introduction of CNO negative electrodes can provide a practical high-rate hybrid device using various perovskites.

## **1. Introduction**

Due to the huge increase in environmental pollution and the excessive use of nonrenewable energies for decades, the development of sustainable energy is required. One of the great challenges facing current researchers is to develop a sustainable and consistent energy supply. The conversion/storage unit is an essential component that ensures an uninterrupted power supply. Li-ion batteries have been established as the dominant energy storage systems, powering almost all electronic devices in the modern world. However, the limited power performance and cycle life, and fire hazards with Li-ion batteries stimulated the research community to consider better alternatives. Electrochemical capacitors (so-called supercapacitors or ultracapacitors) are emerging electrochemical energy storage devices that have many advantages over batteries. Supercapacitors have a higher power density than batteries during charge and discharge and a much higher energy density than conventional dielectric capacitors [1-4]. Thus, several important properties of supercapacitors, such as a high power density and long cycle life, made them favorable for various electronic gadgets and portable electronics. They have found extensive applications in memory backup systems,

consumer electronics, and in the portable electrical industry. Therefore, supercapacitor technology has a high growth rate and is highly reliable where high power supply is demanded. Larger applications, such as regenerative braking, start and stop devices, or emergency opening systems for doors on the Airbus 380 are good illustrations of their implementations as reliable energy storage devices [5].

The electrode materials are the determining component of a supercapacitor. Various types of carbon, binary metal oxides, perovskite oxides, and conducting polymers, have been widely investigated as electrode materials for supercapacitors [6-11]. Each electrode material has its advantages and disadvantages with regard to the targeted application. The carbon-based electrode has a high power density and long cycle life, but a limited specific capacitance. Metal-oxide supercapacitors can provide higher energy density than carbon-based supercapacitors and better cycle stability than conducting polymer capacitors [12]. On the other hand, they have low conductivity and diffusion-limited capacity because of the limited access to active sites within the volume of the electrode material. Hence, it lags far from its expected theoretical capacity, mainly because only surface or sub-surface redox reactions are possible. Several studies have been conducted on metal oxides with various morphologies and compositions to improve the bulk utility of the active sites. Recently, perovskite-type oxide ( $ABO_3$ ) materials have attracted considerable attention to improve the bulk capacity owing to their valence change at the 'B' site transition metal, mobility of the oxygen ion, and electronic conduction along with the three-dimensional  $BO_6$  octahedral network [13,14]. An interesting strategy to circumvent the limited energy density of metal oxides as electrodes for supercapacitors is to design asymmetric hybrid supercapacitors (AHSs) [15]. Recently, hybrid supercapacitors have attracted considerable attention as next-generation power devices for portable electronics and electric vehicles. Hybrid supercapacitors utilize the advantages of both capacitive-type and battery-type electrodes.

Hence, these devices aim to achieve comparable performance to batteries in terms of energy density and to supercapacitors in terms of power density and cycle life. This could be achieved either by hybridizing capacitive and faradaic materials as composite electrodes or by fabricating asymmetric devices combining one battery-type electrode with a capacitive or pseudocapacitive electrode [16, 17]. In this study, a battery-type  $\text{LaMnO}_3$  perovskite was used as a positive electrode, and capacitive rGO and CNO were used as a negative electrode to fabricate hybrid supercapacitor devices.

The properties of perovskite materials are mainly dependent on the ‘A’ and ‘B’ site cations. The perovskite structural tunability offers a wide range of constituent cation substitution by considering the Goldschmidt tolerance factor, which can achieve the formation of the desired composition [14]. To exploit this advantage, the present study adopted a simultaneous partial substitution of the A- and B-sites of  $\text{LaMnO}_3$  perovskite oxide with Sr and Fe, respectively. The Sr-substituted  $\text{LaMnO}_3$  (LSMO) was chosen for two major reasons. First, divalent cation substitution at the trivalent A-site induces a valence change to the transition metal at the B-site from  $\text{B}^{3+}$  to  $\text{B}^{4+}$  to compensate for the charge imbalance. Hence, divalent Sr substitution creates an  $\text{Mn}^{4+}/\text{Mn}^{3+}$  couple that acts as a hopping site for holes in *p*-type conductivity. Second, the substitution of the  $\text{La}^{3+}$  state with  $\text{Sr}^{2+}$  cations increases the tolerance factor and the stability of the perovskite structure [14,8]. On the other hand, the ionic conductivity is still poor, which hinders the application of a high-performance electrochemical energy storage device. The creation of oxygen vacancies inside the crystal lattice is the best way to improve the ionic conductivity. A transition metal at the B-site is oxidized to equilibrate the charge imbalance while substituting the A-site with  $\text{Sr}^{2+}$ . Consequently,  $\text{Mn}^{4+}/\text{Mn}^{3+}$  couples will be formed, which results in enhanced electronic conductivity. At the same time, the formation of  $\text{Mn}^{4+}/\text{Mn}^{3+}$  couples restricts the formation of oxygen vacancies by neutralizing the charge imbalance formed at the A-site due to the

divalent,  $\text{Sr}^{2+}$  substitution for the trivalent,  $\text{La}^{3+}$  cation. Therefore, in this work, Mn was simultaneously substituted with Fe to achieve a mixed ionic-electronic conductivity by controlling the  $3^{+}/4^{+}$  couples. This is expected to lead to a fast positive electrode (battery-type electrode) coupled with a fast capacitive negative one (CNO) to achieve a hybrid supercapacitor exhibiting an interesting tradeoff between the energy and power densities.

## 2. Experimental

### *2.1 Preparation of $\text{LaMnO}_3$ , (Sr, Fe)-substituted- $\text{LaMnO}_3$ , and water-dispersible CNO particles*

The bare and substituted perovskite materials, such as  $\text{LaMnO}_3$ , Sr-substituted  $\text{LaMnO}_3$  ( $\text{LaSrMnO}_3$ ), and Fe-substituted  $\text{LaSrMnO}_3$  ( $\text{La}_{0.7}\text{Sr}_{0.3}\text{Mn}_{(1-x)}\text{Fe}_x\text{O}_3$ ), were prepared using a previously developed synthesis method [19,20]. Lanthanum nitrate ( $\text{La}(\text{NO}_3)_3 \cdot 6\text{H}_2\text{O}$ , 99.999%, Sigma-Aldrich), strontium nitrate ( $\text{Sr}(\text{NO}_3)_2$ , 99.995%, Sigma-Aldrich), manganese sulfate ( $\text{MnSO}_4 \cdot \text{H}_2\text{O}$ , >99%, Sigma-Aldrich), and iron nitrate ( $\text{Fe}(\text{NO}_3)_3 \cdot 9\text{H}_2\text{O}$ , > 99.95%, Sigma-Aldrich) were used as the precursor materials. In a typical synthesis procedure, 0.1 M of the ‘A’ site cation salts and ‘B’ site cation salts were dissolved separately in 10 mL of distilled water under stirring with the appropriate mass proportions. After complete dissolution, the two solutions were transferred to a single beaker, and stirring was continued for 30 minutes. A 10 mL solution of 0.6 M NaOH aqueous solution was prepared separately and poured into the above solution. The solution became brown color instantly with the addition of the NaOH solution. Stirring was continued until the solution developed a dark brown precipitate. The resulting precipitate was then collected and washed several times with distilled water and ethanol followed by centrifugation. The washed sample was finally vacuum-dried at 60 °C overnight. The brown-colored material was made to a powder using a pestle and mortar, and then annealed at 750 °C for 12 h to form highly crystalline  $\text{LaMnO}_3$ -based nanoparticles. The as-prepared  $\text{LaMnO}_3$ ,  $\text{La}_{0.7}\text{Sr}_{0.3}\text{MnO}_3$ ,  $\text{La}_{0.7}\text{Sr}_{0.3}\text{Mn}_{0.9}\text{Fe}_{0.1}\text{O}_3$ ,

$\text{La}_{0.7}\text{Sr}_{0.3}\text{Mn}_{0.7}\text{Fe}_{0.3}\text{O}_3$ ,  $\text{La}_{0.7}\text{Sr}_{0.3}\text{Mn}_{0.5}\text{Fe}_{0.5}\text{O}_3$ ,  $\text{La}_{0.7}\text{Sr}_{0.3}\text{Mn}_{0.3}\text{Fe}_{0.7}\text{O}_3$ ,  $\text{La}_{0.7}\text{Sr}_{0.3}\text{Mn}_{0.1}\text{Fe}_{0.9}\text{O}_3$ , and  $\text{La}_{0.7}\text{Sr}_{0.3}\text{FeO}_3$  were labelled as LMO, LSMO, LSMFO91, LSMFO73, LSMFO55, LSMFO37, LSMFO19, and LSCO, respectively. The pristine carbon nano-onion (CNO) synthesis conditions are reported elsewhere [21].

## **2.2 Material characterizations and modeling**

The crystalline structure of the prepared samples was analyzed by X-ray diffraction (XRD, PANalytical X'Pert-PRO MPD) using  $\text{Cu K}\alpha_1$  (1.5406 Å) over the range from  $10^\circ$  to  $80^\circ$   $2\theta$ . The chemical compositions and oxidation states of each cation were confirmed by X-ray photoelectron spectroscopy (XPS, KRATOS AXIS Supra) using a monochromatic  $\text{Al K}\alpha$  X-ray source (1486.6 eV). The morphology of the prepared materials was examined by field emission scanning electron microscopy (FESEM, Hitachi S-4800) and high-resolution transmission electron microscopy (HR-TEM, TecnaiG2, with  $\text{LaB}_6$  source) with an accelerating voltage of 300 kV. AUTODESK 3DS MAX 2017 and Avogadro version 1.2.0 software were used for atomistic 3D design, modeling, and visualization of both CNO and  $\text{LaMnO}_3$  particles. The proportions of each element in the pure and partially substituted perovskite oxide materials were determined by inductively coupled plasma (ICP), which gives comparatively more accuracy.

The BET surface area and pore size distribution were measured using  $\text{N}_2$  adsorption/desorption (Micromeritics 3-Flex) physisorption analyzer. The electrical conductivity of the electrode materials were measured by the 4-point probe electrical conductivity meter (AIT CMT-100MP), equipped with JANDEL 4-point probe heads. The DC ionic conductivity was estimated using the EIS Nyquist plots obtained from 10 mm diameter pellets which were pressed under a pressure of 30 MPa and coated both sides with Ag as the ion-blocking electrodes. The impedance was measured in the frequency range from 0.1 Hz to 1.0 MHz with 10 mV amplitude using a potentiostat/galvanostat (Metrohm, Autolab PGSTAT 302N).

### ***2.3 Electrodes and device fabrication, and electrochemical characterizations***

The electrochemical properties of the LMO-based materials towards energy storage applications were investigated using a Metrohm, Autolab PGSTAT 302N instrument with three-electrode and two-electrode cell configurations. Cyclic voltammetry (CV), galvanostatic charge-discharge technique (GCD), and electrochemical impedance spectroscopy (EIS) were carried out in a 3 M KOH aqueous electrolyte solution. The working electrodes were fabricated as follows. The active material, carbon black, and PVDF were mixed in a weight ratio of 8:1:1. Initially, the active material and carbon black were ground together using an agate mortar. At the same time, the PVDF was dispersed in the appropriate amount of dimethylformamide (DMF) solution using an ultrasonicator and used to prepare a slurry with the already prepared mixture. The slurry was made homogeneous using a mortar and pestle.

A compressed Ni-foam substrate (1 cm ×1 cm), 85 μm in thickness, was coated with a known weight of the resulting slurry and allowed to dry at 60 °C in a vacuum oven. The substrate was pretreated by chemical etching prior to the mass-loading process. The slurry was coated evenly on the compressed Ni-foam by doctor blade method. This slurry@compressed Ni-foam was used as the working electrode with a mass loading of the active material of 2 to 2.5 mg cm<sup>-2</sup>. An Ag/AgCl reference electrode and a platinum counter electrode were used in a three-electrode cell using a 3M KOH aqueous solution as the electrolyte. CV was carried out at different scan rates, and galvanostatic charge/discharge studies were performed at different current densities. In addition, EIS was performed over a frequency range of 10 mHz to 100 kHz with a potential amplitude of 20 mV. The specific capacity  $Q_{sc}$  (C g<sup>-1</sup>) of an electrode in the three-electrode system was calculated from the GCD curves using Eq. (1):

$$Q_{sc} = \frac{I\Delta t}{m} \quad (1)$$

where  $I$ ,  $\Delta t$ , and  $m$  are the constant current (A), discharge time (s), and total mass of the active material (g), respectively.

The device performance was investigated by fabricating an AHS [15] using a LMO-based electrode as the positive (battery-type electrode) and a CNO-based electrode as the negative (electrochemical capacitor electrode). Both were coated onto Ni-foam as the current collector. Alternatively, a RGO-based electrode was used as the negative for comparison. The two electrodes were separated by glass-fiber paper impregnated with a 3M KOH electrolyte and assembled in a screw-tighten split test cell as an asymmetric design. The specific capacity of the AHS device can be calculated from Eq. (1), with  $m$  for the total mass of active materials in the positive and negative electrodes. Alternatively, when a constant capacitance [22,23] can be calculated for a full AHS, the device capacitance can be obtained from Eq. (2) with  $V$  as the cell voltage.

$$C_{SF} = \frac{2I \int_{V_i}^{V_f} V dt}{m(V_f^2 - V_i^2)} \quad (2)$$

$V_i$  and  $V_f$  denote the lower and upper voltage limits during the discharging process (V), respectively. For the galvanostatic charge/discharge experiments, the C rate is defined as the charge or discharge in one hour. The specific energy  $E$  (Wh kg<sup>-1</sup>) and specific power  $P$  (W kg<sup>-1</sup>) of the AHS device were calculated from Eqs. (3) and (4), respectively.

$$E = \frac{I \int_{V_i}^{V_f} V dt}{3.6m} \quad (3)$$

$$P = \frac{E}{\Delta t} \quad (4)$$

### 3. Result and Discussion

#### 3.1 Materials microstructure and surface chemical compositions

The crystallographic structure and crystallinity were analyzed by powder XRD (Fig. 1a). Rietveld refinement was performed on all the perovskite materials using Fullprof software (program, Full-Prof.2 k, Version 6.10 – Nov2017-ILL JRC) to confirm the crystalline phases. The XRD pattern of LaMnO<sub>3</sub> matched the JCPDS 89-8775 card, which corresponds to the rhombohedral perovskite structure of LaMnO<sub>3</sub> with the R-3c group. The narrow and strong XRD patterns of LaMnO<sub>3</sub> confirmed the highly crystalline nature of the as-synthesized materials. The partial substitution of La (A-site) with the bivalent Sr ion improves the tolerance factor according to the theoretical predictions [14]. All Sr-substituted and Fe-substituted samples exhibited an orthorhombic structure with the Pbnm space group. The substitution of Sr and Fe ions altered the phase from the R-3c group of the rhombohedral perovskite structure to the Pbnm group of the orthorhombic structure. In contrast, Fe<sup>3+</sup> substitution of Mn (B-site) produced some vacancy defects to compensate for the electroneutrality, which was charge-imbalanced by Sr<sup>2+</sup> substitution at the La-site. Such defects increased with increasing rate of Fe substitution.

XPS confirmed the successful elemental substitution, chemical composition, and oxidation states of the “B” cations in LSMO, LSMFO55, and LSFO. Fig. 1b shows the survey spectrum of LSMFO55, where the presence of La, Sr, Mn, Fe, and O was confirmed. Similarly, the presence of Sr on LSMO and LSFO was confirmed from the respective survey spectra (S1a and S1b, respectively). The coexistence of Mn<sup>4+</sup> with Mn<sup>3+</sup> in both LSMO and LSMFO55 was confirmed from the corresponding Mn 2p high-resolution spectra (Figs. S1c and 1c, respectively). The deconvoluted peaks at 641.5 eV and 642.9 eV were assigned to Mn<sup>3+</sup> and Mn<sup>4+</sup> states, respectively [24]. Partial substitution of the divalent Sr<sup>2+</sup> ion for

trivalent  $\text{La}^{3+}$  on the A-site of the parent perovskite structure leaves one additional electron per unit formula,  $\text{ABO}_3$ , which needs to be compensated for by either neutralizing the charge through oxidizing  $\text{Mn}^{3+}$  to  $\text{Mn}^{4+}$  or by producing oxygen vacancies at the anion site. The possibility of this electronic or ionic compensation in the perovskite structure depends mainly on the B-site cation. Therefore, the Sr-substituted  $\text{LaMnO}_3$  compound resulted in the formation of  $(\text{La}_{1-x}^{3+}\text{Sr}_x^{2+}\text{Mn}_{1-x}^{3+}\text{Mn}_x^{4+})\text{O}_3$  owing to the significant change in the valence of the Mn transition metal rather than forming an oxygen vacancy. To conserve charge neutrality, some  $\text{Mn}^{3+}$  ions were oxidized to the  $\text{Mn}^{4+}$  state, as shown in **Fig. S1c**. Unlike Mn metal, Fe metal in the  $\text{LaSrFeO}_3$  structure hinders the oxidation of the B cation but, instead, produces oxygen vacancies. Hence, the amount of  $\text{Mn}^{3+}$  to  $\text{Mn}^{4+}$  conversion was less in LSMFO55 (**Fig. 1c**) than in LSMO (**Fig. S1c**). The mean oxidation state for the LSMFO55 sample was also estimated from the Mn 3s spectrum and the result is compared with the Mn 2p spectrum (**Fig. S1d**). The Mn 3s doublet peak separation is observed to be 5.25 eV, which is nearly the same as the estimated value from the Mn 2p spectrum (3.15 vs 3.18 mean oxidation state of Mn, respectively). The same pattern was observed in the O 1s spectra (**Figs. 1d-1f**), i.e., the ratio of surface adsorbed oxygen ( $\text{OH} + \text{H}_2\text{O}$ ) to the lattice oxygen ( $\text{O}_\text{L}$ ) increase in the order of  $\text{LSMO} < \text{LSMFO55} < \text{LSFO}$ . The peaks observed at 529.3, 531.3, and 533.2 eV corresponded to  $\text{O}_\text{L}$  and OH, and  $\text{H}_2\text{O}$  respectively [25,26]. The latter two are considered as a direct measure of the oxygen vacancies [26,27]. Furthermore, the O1s spectra of pure LMO, LSMO, LSMFO55, LSFO, and  $\text{LaMn}_{0.5}\text{Fe}_{0.5}\text{O}_3$  (LMFO) were compared to confirm the role of the simultaneous substitution of Sr and Fe cations on the generation of oxygen vacancies (**Fig. S2**). The ratio of surface adsorbed oxygen ( $\text{OH} + \text{H}_2\text{O}$ ) to lattice oxygen ( $\text{O}_\text{L}$ ) increased in the order of  $\text{LMO} \approx \text{LMFO} < \text{LSMO} < \text{LSMFO55} < \text{LSFO}$ . The oxygen vacancies in LSMFO were higher than those of LMO, LSMO, and LMFO, showing that an oxygen vacancy is generated due to the simultaneous substitutions of Sr and Fe at the A and B sites, respectively.

The morphology of the different perovskite materials was analyzed by FE-SEM and TEM imaging. **Figs. 2(a)–(d)** present FE-SEM images of LMO, LSMO, LSMFO55, and LSFO, respectively. All four materials exhibited a similar morphology. Agglomeration was observed for all compounds, similar to the “conventional” perovskite oxides, which are normally prepared at higher temperatures [19]. On the other hand, pure  $\text{LaMnO}_3$  showed more particle aggregation than  $\text{La}_{0.7}\text{Sr}_{0.3}\text{Mn}_{0.5}\text{Fe}_{0.5}\text{O}_3$ . **Figs. 2e** and **2f** show TEM and HR-TEM images of LSMFO55, respectively. HR-TEM (**Fig. 2f**) confirmed the crystallinity of the prepared LSMFO compound. Two main crystal lattice fringes were observed (**Fig. 2f**) with interplanar distances of 0.275 nm and 0.195 nm corresponding to the (112) and (220) planes of the orthorhombic pbnm crystal lattice, respectively. The inset figure in **Fig. 2f** represents the selective area electron diffraction (SAED) pattern recorded simultaneously by HR-TEM, suggesting the polycrystalline nature of the LSMFO55 compound. The ICP technique was employed to understand the exact proportion of each element in the pure and partially substituted perovskite oxide materials. Table S1 lists the calculated amounts of different elements for all the prepared samples. The results showed that the predicted elemental proportions of each sample match their calculated values.

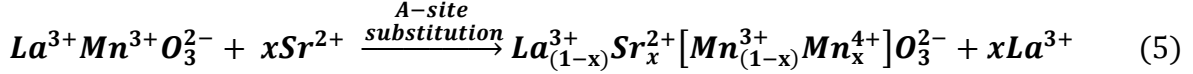
The four-probe electrical conductivity and DC ionic conductivity are shown in Supporting Information (**Fig. S4** and **Table S2**). The DC ionic conductivities of all materials were in good agreement with our theoretical predictions in the next section. The LSMFO55 sample exhibited better conductivity than other materials tested in this study (**Table S2**). The BET surface area and pore size distribution of LSMFO55 are also discussed in Supporting Information (**Fig. S5**). The LSMFO55 sample exhibits a BET surface area of  $19 \text{ m}^2 \text{ g}^{-1}$ , which is in the same order of the literature data ( $10 \text{ m}^2 \text{ g}^{-1}$ ) [13] and is similar to what was obtained in our previous study ( $18 \text{ m}^2 \text{ g}^{-1}$ ) [19] for pure  $\text{LaMnO}_3$ . The average pore size of LSMFO55 is 50 nm. All other electrode materials that we prepared in this study are not expected to have

much deviations from the values for LSMFO55 because (1) the synthesis methods are the same and (2) the morphology turned out similar (Fig. 2).

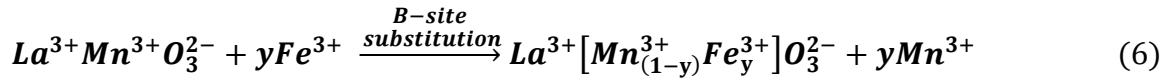
### 3.2 Tuning Electronic and Ionic Conductivities of the LaMnO<sub>3</sub> Perovskite Material

MnO<sub>6</sub> octahedra play a major role in the electronic conductivity of the LaMnO<sub>3</sub> perovskite. Oxygen polarization promotes the formation of a covalent bond between the Mn cation and oxygen anion, which facilitates the electronic conductivity. Electrons of the n-type and holes of p-type perovskites are transported through the Mn–O–Mn chains. The electronic conductivity could be improved further by partial substitution of the A or B site cations with different oxidation states. Furthermore, the ABO<sub>3</sub> perovskite has an inherent property of having oxygen vacancies. These oxygen vacancies will act as a medium for ionic mobility and result in improved ionic conductivity. Therefore, electron/hole conduction along the Mn–O–Mn bond and vacancy-mediated oxygen ion mobility play a major role in mixed ionic-electronic conduction applications. This is being explored for electrodes and ion-conducting electrolytes of various conversion and storage devices [14].

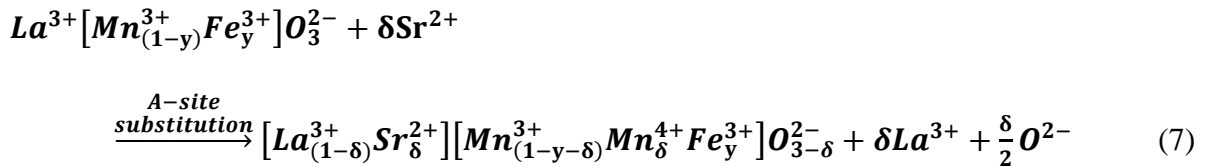
The extensive array of cation substitutions over the La and Mn sites of the LaMnO<sub>3</sub> structure is sufficient to tailor the specific properties. This offers intriguing possibilities for further improvement of the material properties. The A-site cation plays a vital role in tuning these properties. Here, the Sr<sup>2+</sup> (a divalent acceptor) partially substitutes La<sup>3+</sup> (trivalent cation). To maintain the electron neutrality, the effective negative charge induced by Sr<sup>2+</sup> substitution should be balanced either by electronic or ionic compensation. The electronic compensation can readily occur, converting trivalent Mn to tetravalent Mn using the extra electron left at the A site after the Sr<sup>2+</sup> substitution. In other words, the substitution of  $x$  mole of La<sup>3+</sup> by Sr<sup>2+</sup> induces the conversion of  $x$  mole of Mn<sup>3+</sup> to Mn<sup>4+</sup>. Consequently, an electron hole (h<sup>+</sup>) is produced at the tetravalent Mn site and is transported through the Mn–O–Mn chains by p-type conduction. The entire A-site substitution mechanism is described in Eq. (5):



Although the A-site cation plays a vital role in tuning these properties, the B-site cation also has an important role in characterizing the properties of the perovskite materials. When  $y$  mole of  $Mn^{3+}$  in the B-site is substituted by the same amount of  $Fe^{3+}$ ,  $La^{3+}[Mn_{(1-y)}^{3+}Fe_y^{3+}]O_3^{2-}$  is produced.



The ionic compensation occurs when the electronic compensation is restricted by substituting the B-site with another metal ion, such as substitution of  $Mn^{4+}$  with  $Fe^{3+}$ . Because the transition of  $Fe^{3+}$  to  $Fe^{4+}$  is unfavorable, the charge neutrality is achieved by ionic compensation through the formation of oxygen vacancies at the anion sites. In this case, two electron-hole pairs are eliminated by removing a single lattice electron. The mechanism is elucidated by the following reaction (Eq. (7)).



Hence,  $[La_{(1-\delta)}^{3+}Sr_{\delta}^{2+}][Mn_{(1-y-\delta)}^{3+}Mn_{\delta}^{4+}Fe_y^{3+}]O_{3-\delta}^{2-}$  exhibits a combination of electronic and ionic compensation. Consequently, it shows mixed ionic-electronic conductivity. The mechanism is shown schematically in **Fig. 3**.

### 3.3 Materials electrochemistry and device performance

The electrochemical properties of these perovskites were investigated by recording the CV, GCD, and EIS in a three-electrode configuration. Some pretreatment steps were used to avoid the capacity interference from the bare Ni-foam. The capacity contributions of Ni-foam before and after pretreatment were investigated systematically, as shown in **Fig. S3**. The contribution

from the pretreated compressed Ni-foam to the overall capacity was reduced drastically to a negligible level compared to the LSMFO55 electrode. **Fig. 6a** presents the typical CV plots for all perovskite electrodes. For Sr-substituted LaMnO<sub>3</sub> (LSMO), the area bounded by the CV curve increased considerably compared to unsubstituted LaMnO<sub>3</sub> (LMO). This indicates enhanced capacity due to the improved conductivity of the Sr<sup>2+</sup>-substituted LSMO active material. The pronounced redox peaks observed at the positive and negative potential scans reveal faradaic behavior indicative of LSMO as a battery-type electrode. According to literature data, the charge storage mechanism are related to the intercalation of excess oxygen ions into the perovskite structure, where the Mn<sup>3+</sup> oxidizes to Mn<sup>4+</sup> [28]. Furthermore, the simultaneous partial substitution of the B-site with Fe (La<sub>0.7</sub>Sr<sub>0.3</sub>Mn<sub>0.9</sub>Fe<sub>0.1</sub>O<sub>3</sub>) results in a further increase of the current response, thus indicating the enhanced capacity of the Fe-substituted electrode material. Unlike Mn<sup>3+</sup>, the oxidation of Fe<sup>3+</sup> at the B-site to Fe<sup>4+</sup> is unfavorable. Consequently, the charge imbalance produced by Sr<sup>2+</sup> substitution induces oxygen vacancies rather than changing the B-site oxidation state, which resulted in enhanced capacity, as shown in **Fig. 4a**. This characteristic phenomenon was observed until Fe substitution reaches 50%. At the same time, the faradaic capacity contribution from the Fe site was also clearly visible from the CV diagram. This ensures the capacity contribution from the Fe<sup>3+</sup>/Fe<sup>2+</sup> couple along with the Mn<sup>4+</sup>/Mn<sup>3+</sup> [29]. The effect of Fe-substitution on the capacity of other perovskites was also observed in mild aqueous electrolytes [30].

The individual contributions from Fe<sup>3+</sup>/Fe<sup>2+</sup> and Mn<sup>4+</sup>/Mn<sup>3+</sup> couples are systematically proved using XPS analysis and a detailed discussion is included in the next section of this manuscript. The electrode with the composition LSMFO55, exhibited the highest capacity determined from the CV, revealing enhanced gravimetric capacity. At a Fe substitution beyond 50%, the CV loop area decreased upon further substitution of Fe ion at the B-site. A shift of the redox peaks toward a higher potential was observed for the La<sub>0.7</sub>Sr<sub>0.3</sub>FeO<sub>3</sub> electrode. Consequently, the gravimetric capacity decreased with further increase in the substitution level of the Fe ion

at the B-site. Therefore, LSMFO55 displays the largest CV loop area, which indicates that it is the electrode with the most promising performance among the prepared perovskite electrodes.

CV was recorded at various scan rates (2 to 250  $\text{mV s}^{-1}$ ) to study the fast charge transfer kinetics of the LSMFO55 electrode, as shown in **Fig. 4b**. The result was compared with the LSMO and LSFO electrode (**Fig. S6** 'a' and 'b' respectively). In all cases, the CV current response increased with increasing scan rate, indicating the good rate capability of the corresponding electrode materials due to the fast charge transfer kinetics. On the other hand, the redox peaks were observed for the electrodes of LSMO and LSMFO55, even at a higher scan rate of 250  $\text{mV s}^{-1}$ . This was attributed to the minor polarization at the electrode–electrolyte interface, which drastically improves the performance, particularly for fast charging and discharging. **Fig. S5a** displays the polarization versus  $\text{Fe}^{3+}$  substitution. Indeed, most of the electrodes exhibit a mean polarization of about 100 mV between the mean charging and the mean discharging potentials determined from the lowest discharge potential plateau. Only LSMFO55, LSMO73, and LSMFO37, to a minor extent, achieved lowest polarization of 80, 88, and 90 mV, respectively. The superior performance exhibited by the LSMFO55 electrode was attributed to the improved mixed ionic-electronic conductivity of the material through the partial substitution of Sr and Fe ions, respectively. In contrast, the LSFO electrode showed a quite noticeable peak shift at higher scan rates. This was assigned to the purely faradaic nature of the LSFO electrode, where the charge transfer kinetics was diffusion-limited. Hence, at slower scan rates, the electrolyte ions can access maximum active sites in the electrode, while only the surface active sites will be accessible at faster scan rates [31,32].

GCD was performed to examine further the electrochemical energy storage properties of all the prepared electrodes. **Fig. 4c** represents the typical GCD curves corresponding to all electrodes at a current density of 1  $\text{A g}^{-1}$ . The GCD curves also followed the same approach as

observed from their corresponding CV curves. A plateau on the charging and discharging curves was observed for each material, which reflects the faradaic nature of the electrodes. The specific capacity (equation (1)) corresponding to all electrodes was calculated as listed in Table 1. The specific capacity of LSMO was higher than that of the LMO electrode. The substitution of  $\text{Sr}^{2+}$  ions at the  $\text{La}^{3+}$  produced additional electrons, which improved the electronic conductivity of the electrode material. Concomitantly, more sites are available for electron transfer. Moreover, the partial substitution of Fe ions at the B-site improved the ionic conductivity of the electrode material further. Consequently, the LSMFO19, LSMFO37, and LSMFO55 electrodes showed noticeable improvement in capacity compared to the LMO or LSMO counterparts. On the other hand, the further substitution of Fe ions hindered the access of Mn active sites, resulting in a decrease in gravimetric capacity for LSMFO73 and LSMFO93. Among all electrodes investigated in this study, the LSMFO55 electrode exhibited superior gravimetric capacity ( $330 \text{ C g}^{-1}$ , i.e.,  $92 \text{ mAh.g}^{-1}$ ). This may be due to the improved mixed ionic-electronic conductivity of the electrode material. Such capacity is obtained at 12C rate (discharge in 300s). It can be noted that this capacity corresponds to 78% of the theoretical capacity ( $425 \text{ C g}^{-1}$ , i.e.,  $118 \text{ mAh.g}^{-1}$ ) that can be achieved for a one-electron process on the transition metal cationic site thus emphasizing the high rate capability of such electrode. Noticeably, the electrodes with the lowest polarization (LSMFO37, LSMFO55, and LSMFO73) are those with the highest capacity at  $1 \text{ A.g}^{-1}$ . There are also those with the highest percentage of capacity when compared to the theoretical one.

GCD was performed at various current densities (1 to  $15 \text{ A g}^{-1}$ ) to study the charge-discharge behavior of LSMFO55 as shown in **Fig. 4d**. Irrespective of the scan rate, the GCD curve followed a non-linear profile with a tiny plateau portion at the corresponding redox potential (observed from the corresponding CV curve). This was obvious for the superior reversible faradaic reactions, which revealed a battery-type electrochemical charge storage property of the LSMFO55 electrode. The gravimetric capacity of LSMFO55 at different

current densities were calculated and plotted in **Fig. 4e** as a function of the current density. Remarkably, the electrode exhibited excellent rate capability. The specific capacity was maintained at more than 72 % when the current density was increased from 1 to 15 A g<sup>-1</sup>. This translates in 56% of the theoretical capacity that is preserved at 240C, corresponding to a charge or a discharge in 15s.

This excellent rate capability was attributed to the improved mixed ionic-electronic conductivity that was acquired by the simultaneous substitutions of the trivalent La ion (A-site) with divalent Sr ion and of the trivalent Mn ion (B-site) with Fe ion. The results were compared with the LSMO and LSFO electrode (**Figs. S6c–f**), where the rate capability was slightly less for the LSMO electrode and considerably lower for the LSFO electrode. Compared to the capacity measured at 1 A.g<sup>-1</sup>, the LSMO and LSFO electrodes exhibited a rate capability of 54 % and 43 % at a current density of 10 A g<sup>-1</sup>, respectively. This is because the LSMO electrode has a remarkable surface (non-diffusion limited) charge storage contribution along with the diffusion-limited faradaic capacity. In contrast, the LSFO electrode exhibited purely diffusion-limited faradaic behavior, as observed from the CV curve (**Fig. S6a,b**).

A detailed investigation of the charge-transfer kinetics for all electrodes is conducted by EIS, as shown in **Fig. 4f**. Here, the Nyquist plot of each sample depicts three parts. The first part in the high frequency region (the X-intercept) represents the equivalent series resistance ( $R_s$ ).  $R_s$  is a combination of the electrolyte ionic resistance, intrinsic resistance of active material, and the contact resistance between the active material and current collector. The second part corresponds to the charge-transfer resistance ( $R_{ct}$ ) at the electrode–electrolyte interface. The  $R_{ct}$  is usually extracted by measuring the diameter of the semi-circle at a medium frequency region. In the third part, the vertical spike at the lower frequency region represents the frequency-dependent diffusion resistance. **Table 1** lists the measured  $R_s$  and  $R_{ct}$  values for each electrode. The  $R_s$  value was lower for Sr-substituted perovskite electrodes due

to the enhanced electronic conductivity of perovskite obtained by partial substitution of the trivalent La site with the divalent Sr ion. Interestingly,  $R_{ct}$  was the lowest for the LSMFO55 electrode (6  $\Omega$ ) and  $R_s$  was also relatively low (0.39  $\Omega$ ), which resulted in enhanced electrochemical performance of this electrode. We can observe a linear region within the Nyquist plot for the lower frequency region, which is the diffusion part. This is due to the improved mixed ionic-electronic conductivity of the LSMFO55 electrode obtained by substitution of ‘A’ and ‘B’ sites, as stated above. Further, the LSMFO55 electrode was submitted to continuous charge-discharge cycles at a specific current of 5 A g<sup>-1</sup> for 4000 cycles. It exhibited 82% of capacity retention after 4000 cycles. The typical stability plot is presented as **Fig. S7** in supporting information.

### ***3.4 Charge-storage mechanism of the LSMFO55 electrode***

CV was conducted at different scan rates to understand the charge-storage mechanism on the LSMFO55 electrode. The pronounced redox peaks observed in the CV curve (**Fig. 4b**) reflect the direct evidence of ionic diffusion, which contributes mainly to the total capacity of the electrode. In all cases, the current response of the CV curve followed a direct relationship to the scan rate as follows:

$$I = av^b \quad (8)$$

where the current  $I$  obeys a power-law relationship with the scan rate  $v$ . Here,  $a$  and  $b$  are adjustable parameters. For a diffusion-controlled charge-storage process, the peak current ( $I_{pa}$ ) is proportional to the square root of the scan rate. For a non-diffusion-controlled process, for which the charge storage is limited to the surface, the peak current,  $I_{pa}$  is proportional to the scan rate. Hence, the nature of the charge-storage mechanism can be understood by estimating the  $b$  value. **Fig. 6a** presents a plot of the peak current vs. square root of the scan rate for the

LSMFO55 electrode. The good linear relationship with  $R^2 = 0.997$  exhibits a diffusion-limited charge-storage process.

The variation in the  $b$  value can be explained in terms of the diffusion-controlled and surface limited faradaic current response. The current from surface-limited process normally follows a linear dependence on the scan rate. **Fig. 6b** shows the plot of  $\log I$  vs.  $\log \nu$  plot for the LSMFO55 electrode, where  $b$  can be obtained. The slope of the plot was 0.69, located between 0.5 and 1, which shows the presence of noticeable non-diffusion controlled contribution. Hence, the total current can be divided into two categories: diffusion-limited current (typically intercalation of ions in the subsurface or the bulk of the electrode material) and non-diffusion limited process (double-layer capacitance and pseudocapacitance), according to Dunn et al. [33], as given in equation (9). The current response at a fixed potential is the sum of the non-diffusion-controlled processes, mainly surface processes such as double-layer capacitance and faradaic surface charge storage, and diffusion-controlled process.

$$I = k_1\nu + k_2\nu^{1/2} \quad (9)$$

where the first term,  $k_1\nu$ , is the current contribution from the surface-limited effect and the second term,  $k_2\nu^{1/2}$ , describes a diffusion-controlled process related to ion intercalation in the volume of the electrode. The coefficients  $k_1$  and  $k_2$  can be obtained from the slope and y-intercept of the linear  $I/\nu^{1/2}$  vs.  $\nu^{1/2}$  plot. Once the coefficients  $k_1$  and  $k_2$  are known, the individual current contributions can be calculated quantitatively. The contributions of non-diffusion controlled and diffusion-controlled processes to the total current response in CV curves recorded at different scan rates were deconvoluted and are presented in **Fig. 6c**. At a lower scan rate of  $2 \text{ mV s}^{-1}$ , the surface-limited contribution was only approximately 25% of the total current, while the remaining 75% of the total capacity was due to the diffusion-controlled insertion of the electrolyte ion in the bulk of the electrode material. However, the

non-diffusion-limited surface contribution increases gradually as the scan rate increases. At a higher scan rate of  $100 \text{ mV s}^{-1}$ , the major contribution was attributed to the surface effect, i.e., 69% of the total capacity is due to surface-limited charge storage processes. The diffusion-controlled current is limited due to the insufficient time for ions to enter the structure of the material at a higher scan rate. **Fig. 6d** shows the non-diffusion-limited capacity contribution (the shaded region) estimated from the CV curves of the LSMFO55 electrode at a scan rate of  $100 \text{ mV s}^{-1}$ .

The individual contributions from the  $\text{Mn}^{4+}/\text{Mn}^{3+}$  couple and  $\text{Fe}^{3+}/\text{Fe}^{2+}$  couples were distinguished using high-resolution ex situ XPS of both Mn 2p and Fe 2p peaks under charged and discharged conditions to characterize and confirm the valence transition in the process of energy storage. The sample was collected by stopping the reaction once it reaches the maximum potential limit for charged one and minimum potential limit for the discharged one during the whole charge-discharge process at  $1 \text{ A g}^{-1}$  specific current. The transition of  $\text{Mn}^{4+}/\text{Mn}^{3+}$  and  $\text{Fe}^{3+}/\text{Fe}^{2+}$  under normal, charged, and discharged conditions were compared. Both couples contributed considerably to the capacity of the LSMFO55 electrode. **Fig. S9** shows the high-resolution XPS spectrum of Mn 2p and Fe 2p peaks. The oxidation-state profiles derived from these XPS spectra for Mn and Fe is presented in **Figs. 6e and 6f** respectively. The oxidation-state distributions of both Mn and Fe in XPS profile were different at unbiased condition and at charged/discharged conditions. At the normal state (without an applied bias potential), the oxidation-state distribution was  $\text{Mn}^{3+}$  (82%) and  $\text{Mn}^{4+}$  (18%) respectively (**Figs. 6e and S9a**). Whereas, for the charged condition the  $\text{Mn}^{3+}$  was observed to be decreasing (48%) and  $\text{Mn}^{4+}$  increasing (52%), implying that 34% of  $\text{Mn}^{3+}$  is oxidized to  $\text{Mn}^{4+}$  while charging (**Figs. 6e and S9b**). Moreover, the reverse process is observed while discharging (**Figs. 6e and S7c**), indicating the reversible redox reactions at the Mn-site. A similar oxidation-state distribution profile is observed for Fe-site also (**Figs. 6f and S9d-f**). These

results clearly evidence that both the Mn and Fe-site were actively contributing to the charge storage mechanism of the LSMFO55 electrode.

### ***3.5 Design of AHS devices with LSMFO55 as positive electrode***

AHSs were further assembled by combining faradaic LSMFO55 (as a positive electrode) with capacitive CNO and reduced-graphene oxide (rGO) as negative electrodes, namely LSMFO55//CNO and LSMFO55//rGO, respectively. The devices were fabricated in order to explore the practical applications of LSMFO55 perovskite material, which was considered the best electrode from three-electrode system studies and the one with the largest capacity with regards to the theoretical one. The performance of these devices was evaluated by CV, GCD, and EIS. **Figs. 5** and **S8a-h** presents the results of typical electrochemical investigations of LSMFO55//CNO and LSMFO55//rGO AHSs, respectively. The individual electrochemical performances of CNO and rGO electrodes were studied in a three-electrode configuration to maintain the charge balance over positive and negative electrodes of the asymmetric devices. The specific capacitances of CNO and rGO are estimated to be 138 and 95 F g<sup>-1</sup> from **Figs. S8b** and **S8e**, respectively, over a 1V potential window. Based on these evaluations and charge balance calculations [34], the mass loading ratios of CNO and rGO to the LSMFO55 positive electrode were set to 2.5:1 and 3.5:1, respectively. The charge-balanced mass loadings of active materials were calculated based on the capacities obtained from the GCD at 1 A g<sup>-1</sup>. **Fig. 5a** presents the CV plot of LSMFO55//CNO AHS at various scan rates. At low scan rate, a pseudo-rectangular-shaped CV profile is depicted. Such electrochemical signature is awaited from hybrid devices that combine a battery-type electrode as the positive and a capacitive electrode as the negative, LSMFO55 and CNO respectively. Again, the consistent CV profile over a wide range of scan rates indicates the excellent rate capability of the AHS device. However, at fast scan rates (> 100 mV/s), the CVs become distorted, thus indicating a kinetic limitation due to the faradaic positive

electrode. The same behavior was confirmed by recording their corresponding GCD curves (Fig. 5b). The symmetry between the charge–discharge profiles with a low IR-drop confirmed the high electrochemical reversibility and rapid charge transfer kinetics. The gravimetric capacities at various current densities were calculated from the GCD discharge profile using Eq. (1). Fig. 5c demonstrates the specific capacity as a function of the specific current. The LSMFO55//CNO AHS device exhibits a maximum gravimetric capacity of  $104 \text{ C g}^{-1}$  ( $84 \text{ F g}^{-1}$  over 1V voltage window) at a current density of  $1 \text{ A g}^{-1}$ . This value is close to the expected capacity ( $\sim 100 \text{ C.g}^{-1}$ ) from a positive and negative electrode device balance. Interestingly, the device-specific capacity was maintained at  $62 \text{ C g}^{-1}$ , even after increasing the specific current from 1 to  $10 \text{ A g}^{-1}$ , i.e., the device exhibits excellent rate capability (60 %). The practical cell voltage for such AHS is between 0.5 and 1.5V because there is no energy stored below 0.5V, as is often the case for an AHS (Fig. 5a and b).

To ensure the practical application or compare the performance of this AHS with the recently developed devices, the energy and power densities were calculated using equations (3) and (4), respectively. The typical Ragone plot is presented in Fig. 5d. The LSMO55//CNO AHS device delivered an energy density of  $30 \text{ Wh kg}^{-1}$  at a power density of  $1187 \text{ W kg}^{-1}$ . This corresponds to a discharge in 90s (C rate = 40 C). Even at a higher power density of  $10540 \text{ W kg}^{-1}$ , which is approximately a 10-fold higher magnitude than the previous value, the energy density was still maintained at  $17.5 \text{ Wh kg}^{-1}$  (600 C rate). The power and energy densities were compared with the LSMFO55//rGO AHS device, which showed a higher energy density ( $38 \text{ Wh kg}^{-1}$  at a lower power density of  $800 \text{ W kg}^{-1}$ ) than the LSMO55//CNO AHS device. However, the LSMFO55//rGO AHS exhibits a large decrease in energy density while increasing the power density. Interestingly, the LSMO55//CNO AHS device did not show much decrease in energy density at higher power densities. Instead, it maintained moderate energy and power density values. This high rate-performance of LSMO55//CNO AHS can be elucidated by the distinctive selection of an exohedral CNO microstructure as a

negative electrode, which is known for its ultrafast charge–discharge behavior [35,36]. This was attributed to the full accessibility of the CNO surface to electrolyte ions instead of the deep endohedral pores, which were observed in activated carbons and graphene-related materials [36]. These endohedral pores restrict the ion accessibility to their active sites at very fast charge–discharge rates, which eventually reduces the device performance. CNO is a fullerene allotrope and a form of carbon composed of concentric multi-graphene rings, mimicking the morphology of an onion. Furthermore, the 0D exohedral structure, small diameter, high electrical conductivity, and relatively easy aqueous media dispersion, compared to the extensively used 1D nanotubes and 2D graphene, could potentially enhance the electrochemical rate-performance of other oxides/sulfide-based perovskite electrode materials. This excellent consistency is comparable to previously reported high-energy supercapacitor devices and even better than substituted and unsubstituted LMO perovskite-based devices [20,21,37-41].

The life span of a supercapacitor device is another essential parameter, which gauges the long-term application in many low scale (electronic devices) and large scale (automotive, aircraft) applications. Here, the cycling stability of the LSMFO55//CNO AHS device was tested using continuous GCD cycles at  $5 \text{ A g}^{-1}$ . The device exhibited a good stability (86 %) over 7500 cycles, as shown in **Fig. S10**. The high cycling stability and electrochemical reversibility may be a function of the mixed ionic-electronic conductivity of LSMFO55 positive electrode and the exohedral CNO negative electrode, which allows a fully accessible electrode surface for faster ion adsorption–desorption, even at a faster charge–discharge rate. These results confirm that the hybrid battery-type LSMFO55//CNO device can be used as an interesting alternative for the regular metal oxide//carbon AHSs as a high-power device, maintaining its high specific energy and power performance. Moreover, such a device is

operated in a KOH electrolyte, which increases the safety and recyclability compared to organic-based devices.

#### 4. Conclusions

The simultaneous substitution of the A-site La-ion with Sr-ion and the B-site Mn-ion with Fe-ion in  $ABO_3$  perovskite was engineered successfully to achieve a mixed ionic-electronic conductivity, which resulted in very good electrochemical performance of such perovskite electrode. A systematic investigation of different substitution levels of Fe was performed to find the optimal composition to achieve higher electrochemical performance. The 30 % A-site and 50 % B-site substituted perovskite (LSMFO55) electrode exhibited a superior battery-type storage property with a specific capacity of  $330 \text{ C g}^{-1}$  at 12C cycling rate, implying the best candidate material among the fabricated perovskite electrodes. Such capacity is 78% of the theoretical capacity of the electrode material. Moreover, the non-diffusion limited current (due mainly to the surface faradaic reactions) and diffusion-limited current contributions in the CV curve of the LSMFO55 electrode were deconvoluted. The hybrid battery-type LSMFO55//CNO asymmetric hybrid supercapacitor (AHS) device exhibited very good performance with an excellent rate capability and long-term cycling stability. The AHS device delivered a high energy density of  $30 \text{ Wh kg}^{-1}$  at a power density of  $1187 \text{ W kg}^{-1}$ , maintaining the energy density above 60% even at a high power density of  $10.5 \text{ kW kg}^{-1}$ . These results suggest that the tuning of mixed ionic-electronic conductivity by successful cationic substitutions at the 'A' and 'B' sites of the  $ABO_3$ -type perovskite electrode could enhance the electrochemical performance significantly. In particular, LSMFO55 electrode was found to be the best choice of material for an efficient, positive electrode for battery-type supercapacitor applications. In addition, the combination of LSMFO55 as a positive electrode and CNO as a negative electrode is a remarkable example for efficient and stable hybrid devices.

## Acknowledgments

This study was supported by the National Research Foundation (NRF) of the Republic of Korea under the frameworks of the Priority Research Centers Program (NRF-2014R1A6A1031189) and the Regional University Superior Scientist Research Program (NRF-2020R1I1A3073981) funded by the Ministry of Education, the Republic of Korea.

## References

- [1] A.K. Samantara, S. Ratha, *Materials Development for Active/Passive Components of a Supercapacitor: Background, Present Status and Future Perspective*, Springer, **2017**.
- [2] M.A. Scibioh, B. Viswanathan, *Materials for Supercapacitor Applications*, Elsevier, **2020**.
- [3] M. Winter, R.J. Brodd, What are batteries, fuel cells, and supercapacitors? *Chem. Rev.*, **2003**, 104, 4245; *ibid.* 2004, 105(3) 1021.
- [4] B.E. Conway, W.G. Pell, *J. Solid State Electrochem.* **2003**, 7, 637.
- [5] P. Simon, Y. Gogotsi, A. Schneuwly, R. Gallay, *Nat. Mater.* **2008**, 7, 845.
- [6] P.-C. Chen, G. Shen, Y. Shi, H. Chen, C. Zhou, *ACS Nano* **2010**, 4, 4403.
- [7] P.B. Karandikar, D.B. Talange, U.P. Mhaskar, R. Bansal, *Energy* **2012**, 40, 131.
- [8] A. Balducci, R. Dugas, P.-L. Taberna, P. Simon, D. Plee, M. Mastragostino, S. Passerini, *J. Power Sources* **2007**, 165, 922.
- [9] M. Mastragostino, C. Arbizzani, F. Soavi, *Solid State Ion.* **2002**, 148, 493.
- [10] X. Xu, S. Li, H. Zhang, Y. Shen, S.M. Zakeeruddin, M. Graetzel, Y.-B. Cheng, M. Wang, *ACS Nano* **2015**, 9, 1782.
- [11] G.A. Snook, P. Kao, A.S. Best, *J. Power Sources* **2011**, 196, 1.
- [12] H. Jiang, J. Ma, C. Li, *Adv. Mater.* **2012**, 24, 4197.
- [13] J.T. Mefford, W.G. Hardin, S. Dai, K.P. Johnston, K.J. Stevenson, *Nat. Mater.* **2014**, 13, 726.

- [14] J. Richter, P. Holtappels, T. Graule, T. Nakamura, L.J. Gauckler, *Monatsh.Chem.* **2009**, *140*, 985.
- [15] WG Pell, BE Conway, *Journal of Power Sources*, 2004, *136*(2):334–345
- [16] George Z. Chen, *International Materials Reviews*, 2017, *62*(4), 173-202.
- [17] F. Béguin, E. Frąckowiak (eds), *Supercapacitors – Materials, Systems, and Applications*, Wiley-VCH Verlag GmbH & Co. KGaA, Weinheim, Germany, 2013.
- [18] S. Jiang, *Solid State Ion.* **2002**, *146*, 1.
- [19] P.M. Shafi, N. Joseph, A. Thirumurugan, A.C. Bose, *Chem. Eng. J.* **2018**, *338*, 147.
- [20] P.M. Shafi, A.C. Bose, A. Vinu, *ChemElectroChem* **2018**, *5*, 3723.
- [21] D. Mohapatra, S. Badrayyana, S. Parida, *Mater. Chem. Phys.*, **2016**, *174*, 112-119.
- [22] T Brousse, D Bélanger, JW Long, *J. Electrochem. Soc.* 2015, *162*(5), 5185-5189.
- [23] A. Balducci, D. Belanger, T. Brousse, J. W. Long and W. Sugimoto *J. Electrochem. Soc.* 2017, *164*(7), 1487-1488.
- [24] J.F. Moulder, Handbook of X-ray photoelectron spectroscopy, Physical Electronics, (1995) 230.
- [25] M. Wegmann, L. Watson, A. Hendry, *J. Am. Ceram. Soc.* **2004**, *87*, 371.
- [26] C. Zhang, C. Wang, W. Zhan, Y. Guo, Y. Guo, G. Lu, A. Baylet, A. Giroir-Fendler, *Appl. Catal.* **2013**, *129*, 509.
- [27] H. Yang, J. Zhang, G. Lin, T. Xian, J. Jiang, *Adv. Powder Technol.* **2013**, *24*, 242.
- [28] Z.A. Elsiddig, H. Xu, D. Wang, W. Zhang, X. Guo, Y. Zhang, Z. Sun, J. Chen, *Electrochim. Acta* **2017**, *253*, 422.
- [29] X. Chen, K. Chen, H. Wang, D. Xue, *J. Colloid Interf. Sci.* **2015**, *444*, 49.
- [30] P. Lannelongue et al. *Electrochim. Acta*, 2018, *271*, 677-684
- [31] M. Toupin, T. Brousse, D. Bélanger, *Chem. Mater.* **2002**, *14*, 3946.
- [32] S. Chaudhari, D. Bhattacharjya, J.-S. Yu, *RSC Adv.* **2013**, *3*, 25120.
- [33] T. Brezesinski, J. Wang, S.H. Tolbert, B. Dunn, *Nat. Mater.* **2010**, *9*, 146.

- [34] P.M. Shafi, V. Ganesh, A.C. Bose, *ACS Appl. Energy Mater.* **2018**, *1*, 2802.
- [35] D. Mohapatra, G. Dhakal, M.S. Sayed, B. Subramanya, J.-J. Shim, S. Parida, *ACS Appl. Mater. Interfaces* **2019**, *11*, 8040.
- [36] D. Pech, M. Brunet, H. Durou, P. Huang, V. Mochalin, Y. Gogotsi, P.-L. Taberna, P. Simon, *Nat. Nanotechnol.* **2010**, *5*, 651.
- [37] X. Lang, H. Mo, X. Hu, H. Tian, *Dalton Trans.* **2017**, *46*, 13720.
- [39] H. Mo, H. Nan, X. Lang, S. Liu, L. Qiao, X. Hu, H. Tian, *Ceram. Int.* **2018**, *44*, 9733.
- [39] S. Nagamuthu, S. Vijayakumar, K.-S. Ryu, *Mater. Chem. Phys.*, **2017**, *199*, 543.
- [40] D. Moitra, C. Anand, B.K. Ghosh, M. Chandel, N.N. Ghosh, *ACS Appl. Energy Mater.* **2018**, *1*, 464.
- [41] H. Fan, R. Niu, J. Duan, W. Liu, W. Shen, *ACS Appl. Mater. Interfaces.* **2016**, *8*, 19475.

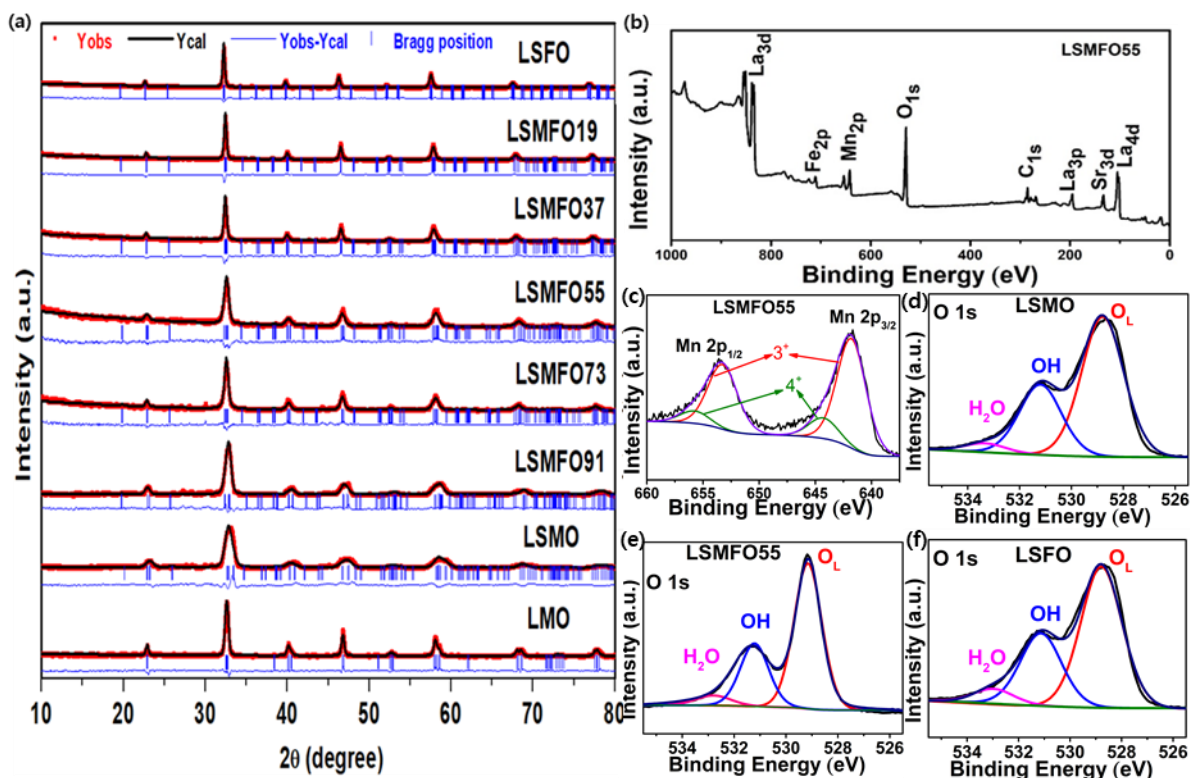


**Fig. 1** a) XRD profile with Rietveld refinement of unsubstituted and substituted  $\text{LaMnO}_3$  perovskites; b) XPS survey spectrum of LSMFO55; c) XPS Mn 2p spectrum of LSMFO55; d-f) O 1s spectrum corresponding to LSMO, LSMFO55 and LSFO, respectively.

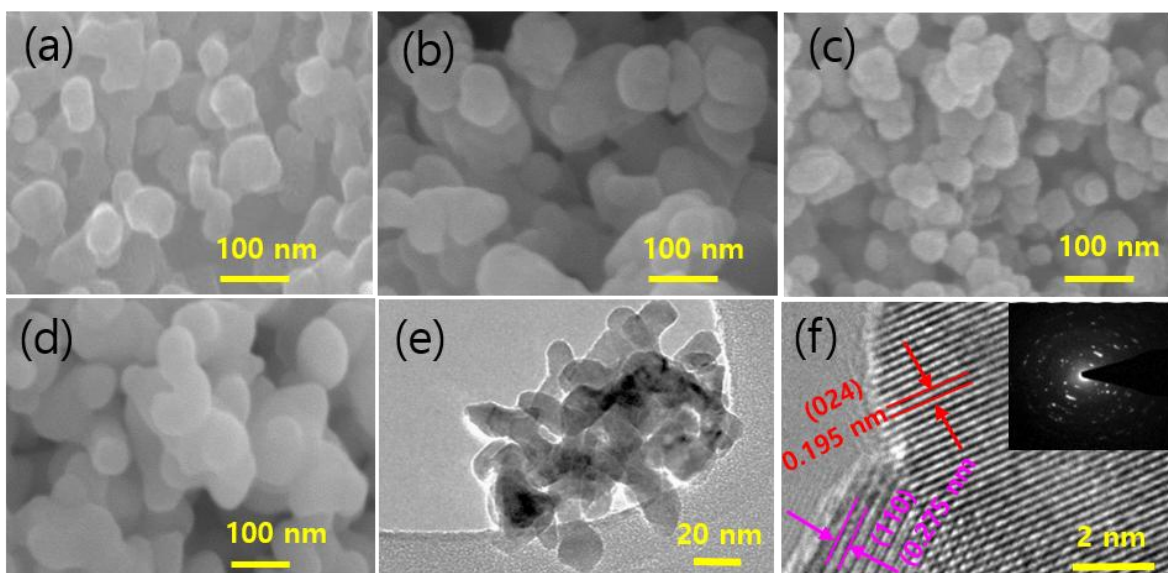


**Fig. 2** FE-SEM images of (a)  $\text{LaMnO}_3$  (LMO) (b) LSMO (c) LSMFO55 and (d) LSFO; (e) and (f) correspond to TEM and HR-TEM images of LSMFO55, respectively (inset of (f): corresponding SAED pattern).

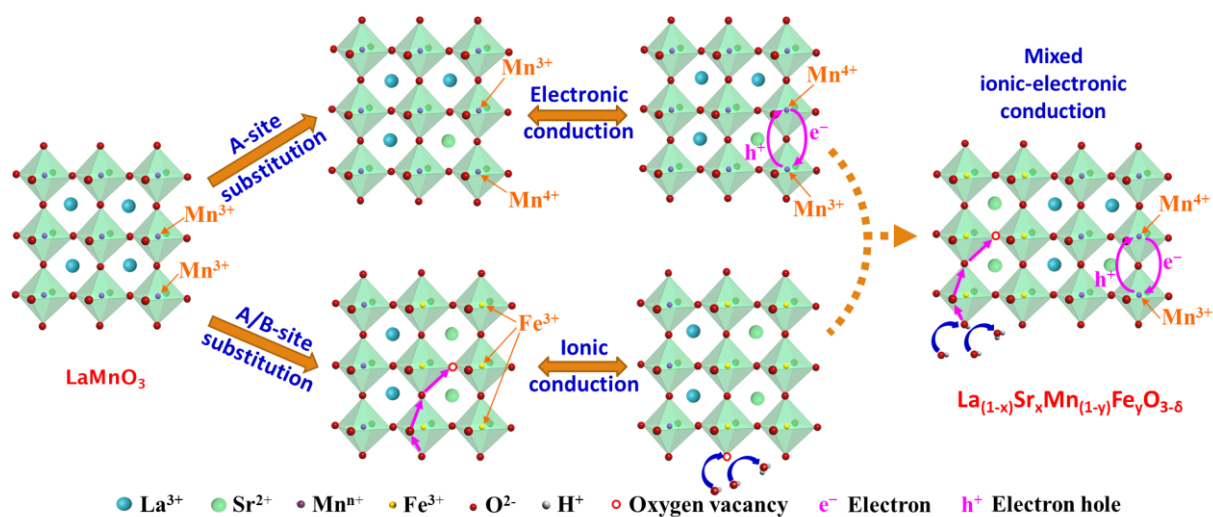


**Fig. 3** Schematic diagram for tuning mixed ionic-electronic conductivity by A and B-site substitution.

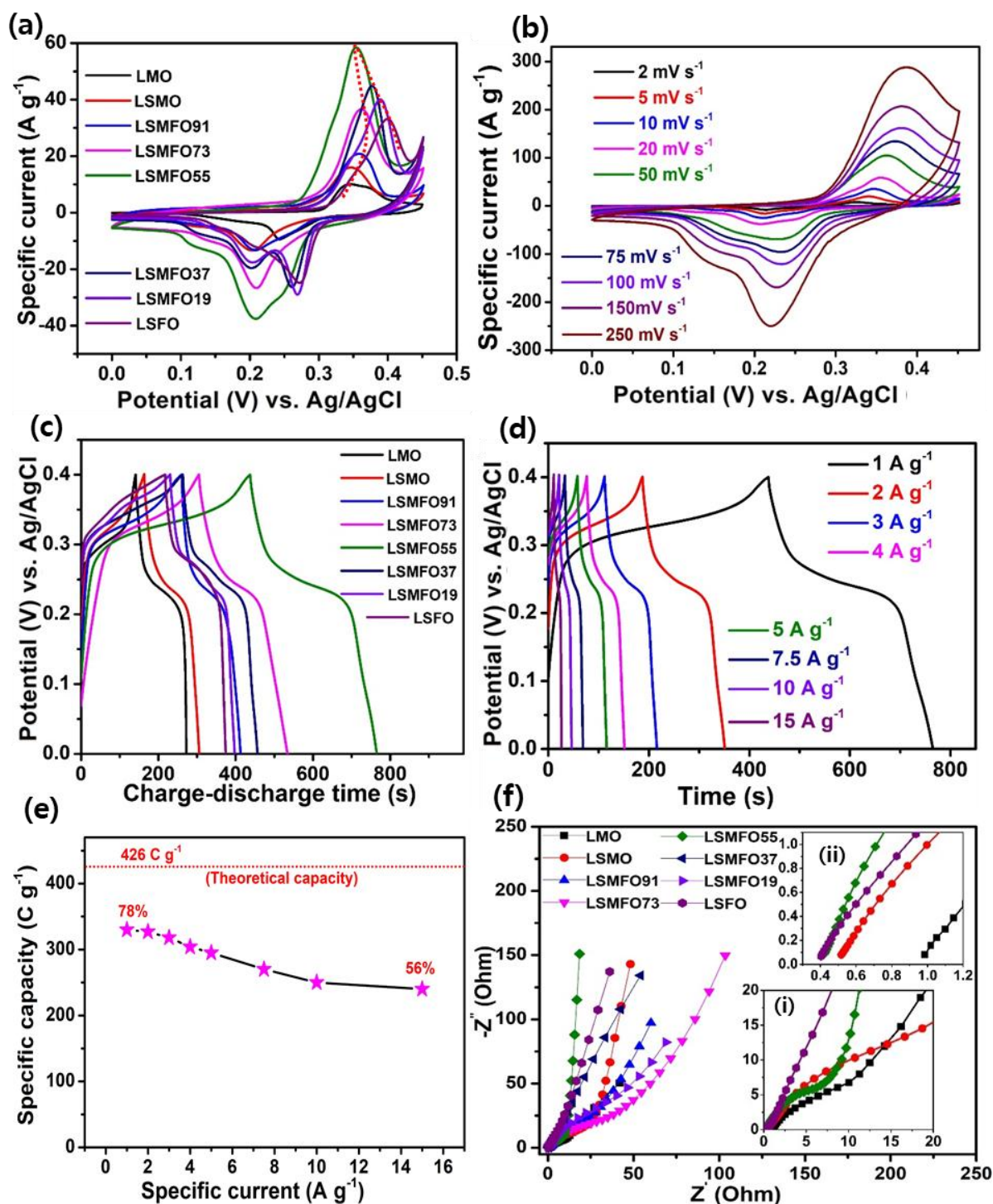


**Fig. 4** (a) CV plot recorded at a scan rate of  $20 \text{ mV s}^{-1}$  for all samples in 3M KOH electrolyte (dashed lines are a guide for the eyes to indicate the peak shift), (b) CV curve of LSMFO55 at different scan rates, (c) charge-discharge curves recorded for all samples at a current density of  $1 \text{ A g}^{-1}$ , (d) GCD curve of LSMFO55 at various current densities, (e) capacity retention plot recorded at higher current densities corresponding to LSMFO55 electrode, and (f) EIS recorded for all eight electrodes.

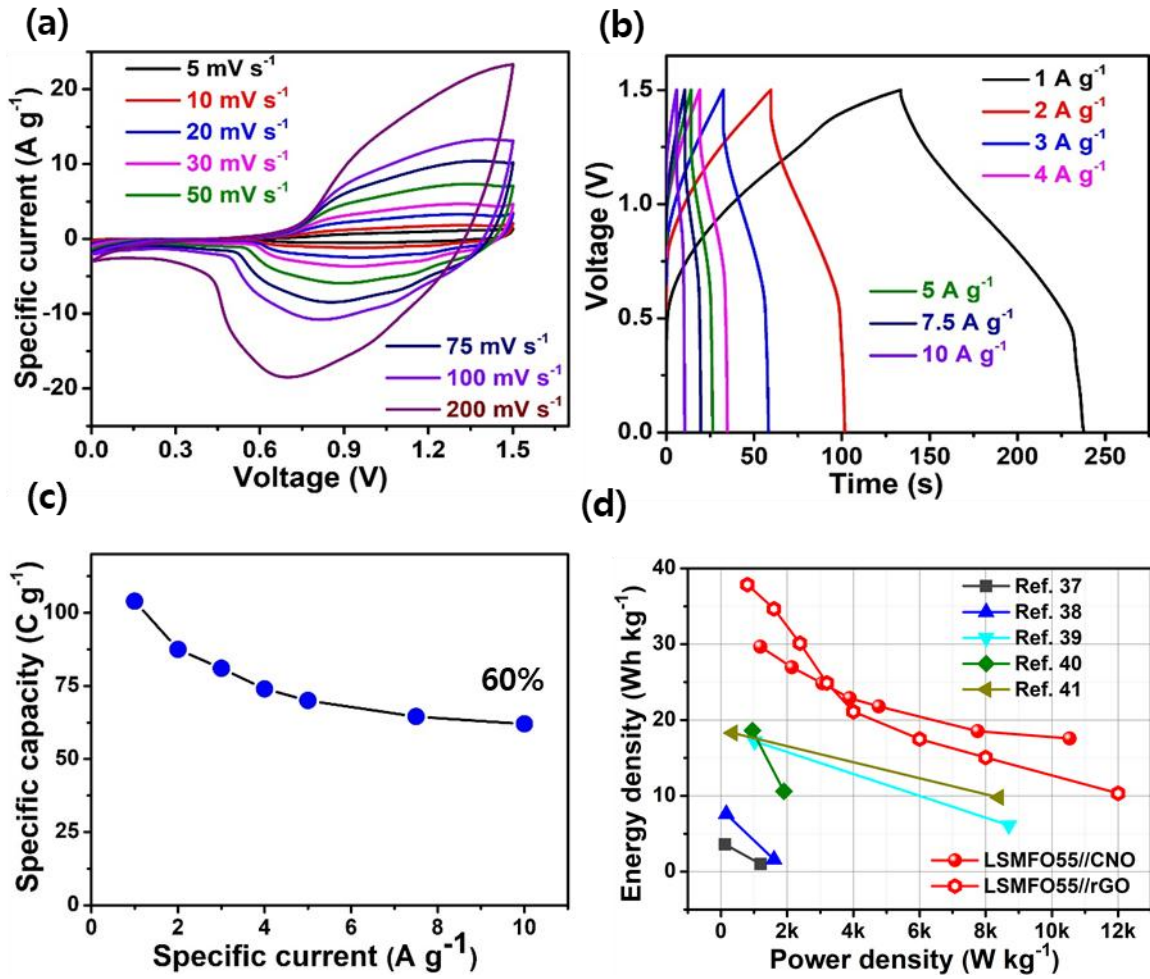


**Fig. 5** Electrochemical performance of LSMFO55//CNO hybrid device operated in 3M KOH electrolyte: (a) CV at different scan rates, (b) GCD at different current densities, (c) capacity retention at higher current densities, and (d) Ragone plot.

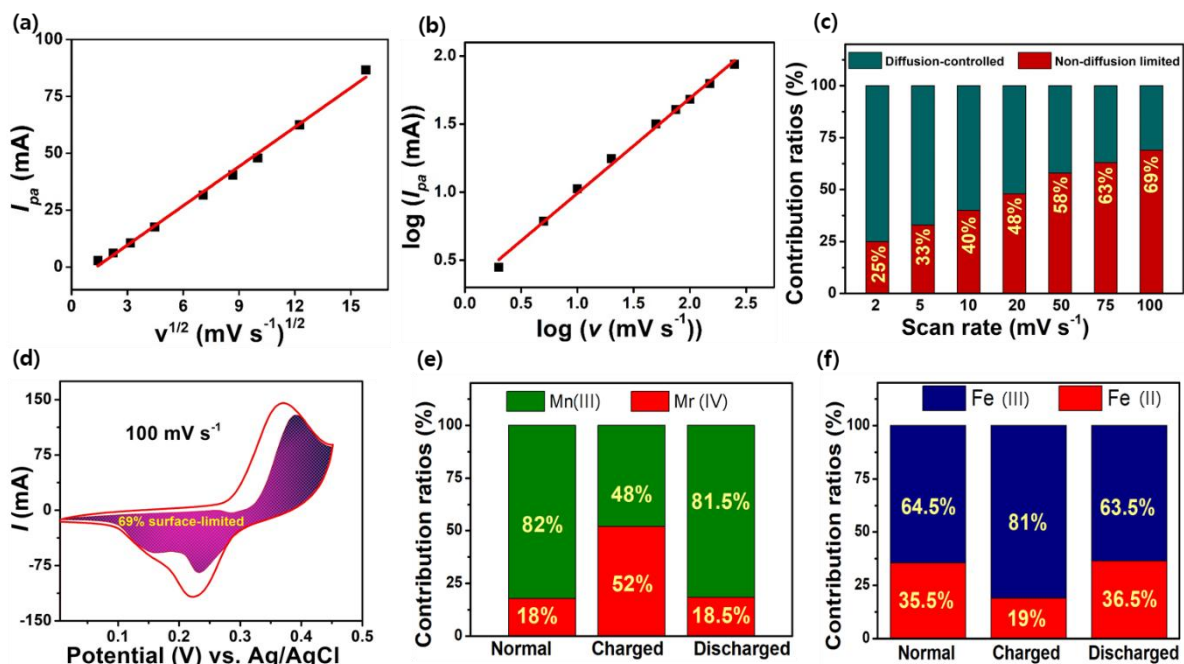


**Fig. 6** (a) Peak current ( $I_{pa}$ ) vs. square root of the scan rate ( $v^{1/2}$ ), (b)  $\log I$  vs.  $\log v$  plot, (c) non-diffusion limited contributions at different scan rates, and (d) Dunn's plot corresponding to the scan rate of  $100 \text{ mV s}^{-1}$  for the LSMFO55 electrode. Oxidation-state profiles by XPS of (e) Mn and (f) Fe at various potentials.

**Table 1.** Estimated values of the  $R_s$  and  $R_{ct}$  from the Nyquist plot and the theoretical specific capacity ( $Q_{th}$ ) along with the measured specific capacity ( $Q_{meas}$ ) calculated from the GCD data obtained at  $1 \text{ A.g}^{-1}$ .

Electrode	$R_s$ (Ohm)	$R_{ct}$ (Ohm)	$Q_{th}$ ( $\text{C g}^{-1}$ )	$Q_{meas}$ ( $\text{C g}^{-1}$ )	$Q_{meas}/Q_{th}$ (%)
LMO	0.95	8	399	130	33
LSMO	0.51	20	426	145	34
LSMFO91	0.81	14	426	153	36
LSMFO73	0.25	13	426	230	54
LSMFO55	0.39	6	425	330	78
LSMFO37	0.30	9	425	194	46
LSMFO19	0.30	12	425	171	40
LSFO	0.4	7.5	424	160	38

## Table of Contents

The rate capability of LSMFO55//CNO AHS device was drastically enhanced by improving the **mixed ionic-electronic conductivity** of perovskite material and introducing the exohedral carbon nano-onion (CNO) as a negative electrode. The ionic size and chemical properties of the substituent cation played a significant role in the material symmetry and the performance of the hybrid device.

*P. Muhammed Shafi, Debananda Mohapatra, V. Pradeep Reddy, Ganesh Dhakal, Deivasigamani Ranjith Kumar, Dirk Tuma, Thierry Brousse\*, Jae-Jin Shim\**

